Form Drag and Mixing Due to Tidal Flow past a Sharp Point

KATHLEEN A. EDWARDS

Applied Physics Laboratory, University of Washington, Seattle, Washington

PARKER MACCREADY

School of Oceanography, University of Washington, Seattle, Washington

JAMES N. MOUM

College of Ocean and Atmospheric Sciences, Oregon State University, Corvallis, Oregon

GENO PAWLAK

School of Ocean and Earth Science and Technology, University of Hawaii at Manoa, Honolulu, Hawaii

JODY M. KLYMAK AND ALEXANDER PERLIN

College of Ocean and Atmospheric Sciences, Oregon State University, Corvallis, Oregon

(Manuscript received 12 May 2003, in final form 10 October 2003)

ABSTRACT

Barotropic tidal currents flowing over rough topography may be slowed by two bottom boundary–related processes: tangential stress of the bottom boundary layer, which is generally well represented by a quadratic drag law, and normal stress from bottom pressure, known as form drag. Form drag is rarely estimated from oceanic observations because it is difficult to measure the bottom pressure over a large spatial domain. The ''external'' and ''internal'' components of the form drag are associated, respectively, with sea surface and isopycnals deformations. This study presents model and observational estimates of the components of drag for Three Tree Point, a sloping ridge projecting 1 km into Puget Sound, Washington. Internal form drag was integrated from repeat microstructure sections and exceeded the net drag due to bottom friction by a factor of 10–50 during maximum flood. In observations and numerical simulations, form drag was produced by a lee wave, as well as by horizontal flow separation in the model. The external form drag was not measured, but in numerical simulations was found to be comparable to the internal form drag. Form drag appears to be the primary mechanism for extracting energy from the barotropic tide. Turbulent buoyancy flux is strongest near the ridge in both observations and model results.

1. Introduction

Enhanced oceanic mixing at coastal boundaries results from the conversion of the kinetic energy of the barotropic tidal current into internal waves and vortical eddies. These structures evolve into 3D turbulence and are a mechanism for mixing stratified water in the interior. There is also direct mixing of stratified water within the turbulent bottom boundary layer, particularly where isopycnals intersect sloping sidewalls (Garrett et al. 1993). The net rate at which these boundary mechanisms remove energy from the barotropic flow is the scalar product of the free-stream velocity and the area-integrated boundary stress (Gill 1982, p. 311). The latter is a combination of frictional stress from the classical turbulent bottom boundary layer and form drag due to pressure differences across topographic features (Kundu and Cohen 2002, p. 338; Baines 1995, p. 13). The goal of this study is to present observations and numerical simulations relevant to this conversion process. We focus on several tidal cycles of flow past a sloping ridge (Fig. 1), Three Tree Point (TTP; Fig. 2), which is a site of high drag and turbulent mixing.

In considering the form drag caused by TTP, we define ''internal form drag'' to be that produced by the deformation of isopycnals in stratified flow, while ''external form drag'' is generated by deformation of the sea surface. When the obstacle is a sloping ridge, form drag

Corresponding author address: Parker MacCready, School of Oceanography, University of Washington, Box 355351, Seattle, WA 98195-5351.
E-mail: parker@ocean.washington.edu

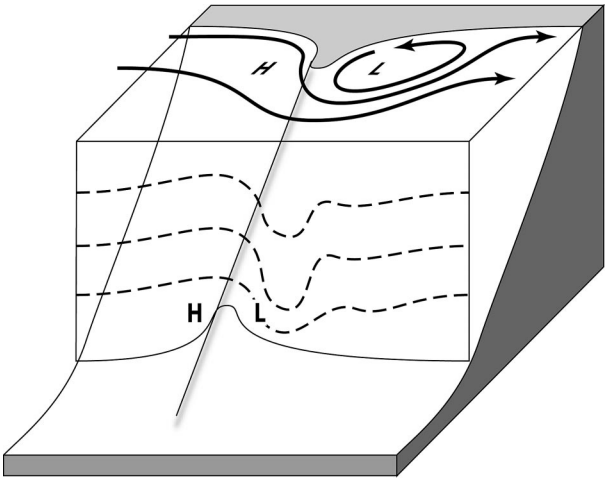

FIG. 1. Schematic of the two mechanisms for creating form drag from a sloping ridge: wave generation (dashed isopycnals) and flow separation (solid streamlines). Both can occur at the surface (external form drag) or at depth (internal). Associated positive (negative) pressure perturbations are labeled with H (L).

can be produced by two mechanisms, flow separation and wave generation (Fig. 1), which can occur at the surface or within the water column. Both mechanisms result in high pressure upstream of the obstacle and low downstream, but are distinguished by the flows they produce. For lee wave generation, high speeds are found downstream of the obstacle while for flow separation, they are found upstream. Depending on the flow regime, these two mechanisms can occur separately or together (MacCready and Pawlak 2001), as they do in the current study.

Form drag is ubiquitous in geophysical flows, and much of our understanding comes from studies of airflow over mountains. Smith (1978) measured the form drag on a small mountain using a number of microbarographs at ground stations. To avoid errors due to uncertainty in the absolute height of the instrument, he selected periods of negligible winds and assumed that these observations recorded absolute pressures. Other estimates of mountain form drag have built on this approach, or on aircraft measurements of vertical momentum fluxes (see Davies and Phillips 1985 for a review). For example, Hafner and Smith (1985) used a 2D microbarograph array to estimate form drag vectors across the Alps, rather than assuming that the drag always acts normal to a ridge crest. The topographic drag exerted on the atmosphere can be substantial, ranging from nearly equal to the frictional drag to 10 times its value for the Southern Alps of New Zealand. A mountain lee wave in Lilly (1978) generated form drag of magnitude equal to a third of the global average drag at the mountain's latitude. Since the flows which generate form drag are typically of much smaller scale than those resolved by atmospheric numerical models, there has been considerable work on its parameterization, which Lott and Miller (1997) found to improve predictions of flow over mountains. Both the physics and the forecasting implications are reviewed by Schär (2002).

In contrast with atmospheric studies, oceanic estimates of form drag are rare because it is difficult to make highly spatially resolved bottom pressure measurements across an underwater obstacle. One of the few oceanic measurements of form drag due to lee wave generation was made by Moum and Nash (2000) and Nash and Moum (2001) at Stonewall Bank off the Oregon coast. On this 5-km-long obstacle, form drag exceeded skin friction by a factor of 2–3. The form drag estimate was based on vertically integrated density profiles from the free-falling Chameleon profiler, as it is in the results presented here. Since the upper layer of the two-layer flow was nearly stationary, the sea surface slope, and thus external form drag, could be assumed to be negligible. Here, we will estimate the external form drag numerically for comparison to the other components of the boundary stress.

In addition to lee wave generation, form drag can also be generated by flow separation, and several studies have addressed this mechanism in the ocean. Most have focused on cases in which the flow is relatively shallow and 2D. Wolanski et al. (1984) found that sea level upstream of Rattray Island exceeded values in a downstream separation region by 2.5 cm. Signell and Geyer (1991) showed that modeled flow separation at a coastal headland was associated with a difference in surface height of several centimeters and depended on the relative sizes of scales for the topography, frictional decay, and tidal excursion. In Knight Inlet, Klymak and Gregg (2004) estimated that radiating internal waves were the major sink for barotropic tidal energy, followed by headland vortices then bottom friction and internal turbulence. The vortices were generated by boundary layer separation (Klymak and Gregg 2001). The cruise described in the current study was followed by others that recorded the surface height and headland eddy shedding at TTP (Pawlak et al. 2003); these later observations allow the external form drag component due to flow separation to be calculated, which is only done numerically here.

Given the observational difficulties, numerical studies have provided useful insights into the mechanics of form drag. The increase of the form drag with the height of an isolated ridge on a slope has been simulated by MacCready and Pawlak (2001) using the same model that will be used in the present study. The authors found that the pressure drag coefficient in wave generation and flow separation regimes was similar, and that this drag coefficient, referenced to the projected frontal area of the ridge, could be $O(1)$. In a numerical simulation of flow over the corrugated continental slope near Porcupine Bank off England, Thorpe (1992) found that frictional and form drag contributed equally to net drag.

Numerical models of barotropic tidal flow in the site of our study, Puget Sound (Lavelle et al. 1988), and the

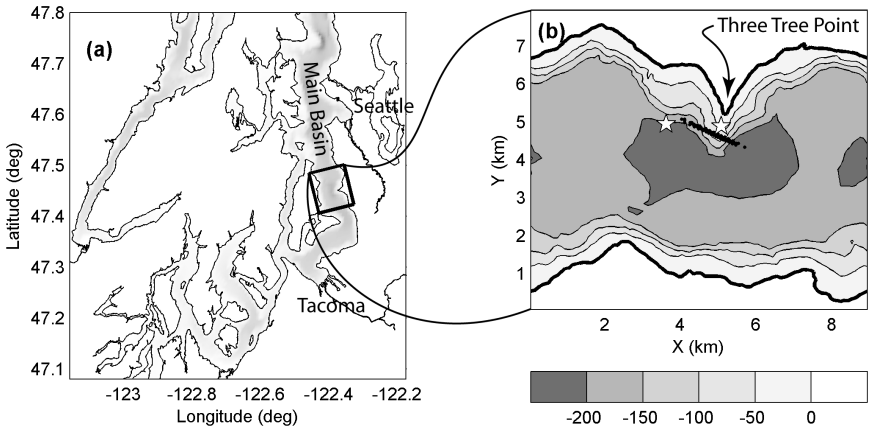

FIG. 2. Maps of (a) Puget Sound, WA, and (b) Three Tree Point. A local, rotated coordinate system (x, y) is defined in (b) such that flood tide produces positive along-channel flow (to the right). The spatial domain of the numerical model is depicted in (b); its bathymetry (m) is shown by the grayscale. The line of dots crossing TTP at an angle shows the locations of microstructure profiler drops. The locations of two bottom-mounted ADCP moorings are shown by stars.

Strait of Juan de Fuca (Foreman et al. 1995), have required a quadratic drag coefficient of $\sim 1\text{–}2 \times 10^{-2}$ in order to match observed patterns of tidal height and phase. This is 5–10 times typical values in regions lacking rough topography, and based on the results of the current study, we speculate that this is due to form drag on unresolved topography. The spatial scale of topographic obstacles that cause the greatest oceanic form drag is not well known but is likely to lie between the scale at which an obstacle begins to protrude out of the bottom boundary layer ($\sim$20 m) and the scale at which geostrophy begins to noticeably affect the flow ($\sim$10 km). The importance of form drag in the ocean has recently been highlighted by the observation of enhanced mixing high over the Mid-Atlantic Ridge, presumably driven by the conversion of barotropic tidal flow across the ridge into internal waves (Ledwell et al. 2000; Jayne and St. Laurent 2001).

Insight into the currents at TTP comes from analysis of 31 days of National Oceanic and Atmospheric Administration (NOAA) current-meter observations made in 1983 on a cross-channel section (Bretschneider et al. 1985). In an EOF analysis of the subtidal current structure, the authors found that the surface currents above $\sim$20 m responded to the wind, while the deepest currents were driven by up-estuary propagation of overflows of dense Pacific water. Intensified at middepth (20–60 m) and on the TTP side of the channel, a subtidal current flowed southward during spring tides and was attributed to a clockwise circulation around Vashon Island resulting from tidal rectification (Barnes and Ebbesmeyer 1978). No instruments were placed close to TTP in the upper 100 m, however, and so the subtidal current structure there was not resolved. Tidal time-scale analysis of these observations (Lavelle et al. 1988, their Figs. 19–20) showed that the amplitude of the along-channel M_2 currents ranged from 10 cm s^{-1} on the western half of the channel to 23 cm s^{-1} near TTP. There was also a phase lead of 50° (1.7 h) in the deep water near TTP relative to the surface. This phase lead is typical of headlands (Geyer and Signell 1990) or of any first-order ODE with periodic forcing and some damping.

As reviewed in Belcher and Hunt (1998), topographical obstacles can greatly alter the mean and turbulent properties of the flow. Our presentation of an example of this at TTP is organized as follows. Section 2 describes the TTP observations and the numerical model setup. Results presented in section 3 include a comparison of high observed and modeled turbulent buoyancy flux, and tidally varying estimates of the frictional and form drag. A key finding is that the form drag dominates the total drag exerted by TTP. In section 4, the high drag coefficients required to model the region are discussed in relation to the form drag results, and section 5 lists conclusions.

2. Methods

a. Observational analysis

The study site, TTP, is a sharp headland that juts out 1 km from the walls of Puget Sound, Washington (Fig. 2). It was selected for its relatively regular shape and isolation from other features. Subsurface, TTP is a ridge sloping downward at a slope of $\sim$1:5 (vertical:horizontal), permitting flow to pass both over and around it, as sketched in Fig. 1. The Main Basin of Puget Sound typically has steep sidewalls and a flat bottom at 200 m due to sedimentary infill of the glacially carved channel. The 30-m depression off the toe of TTP is common to many headlands around Puget Sound and may reflect

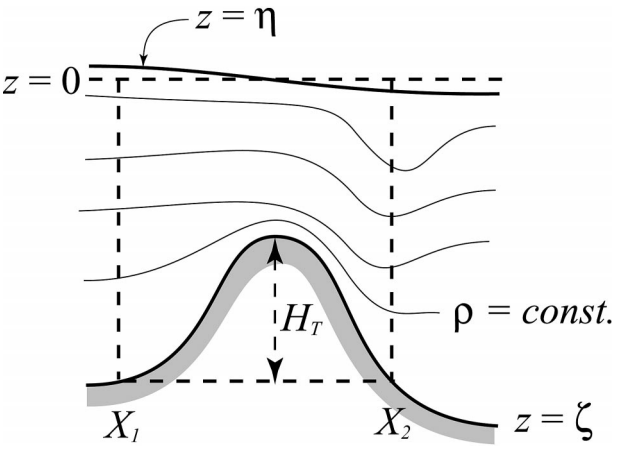

FIG. 3. Schematic of stratified flow past a bump of height H_T. The form drag is integrated from X_1 to X_2, where the bottom depths are equal. Because of both the surface tilt and the isopycnal deflection, the bottom pressure, p_B, would be higher on the left side of the bump relative to the right, leading to a form drag that would push to the left.

preferential lack of sediment deposition because of enhanced tidal currents.

In March of 2001, the R/V *Thomas G. Thompson* conducted the first of several cruises at TTP. Results from later cruises will be published separately. Over 1.5 days, the *Thompson* completed nine repeat sections along the track shown in Fig. 2 in order to make flow and turbulence measurements over the tidal cycle. Lavelle et al. (1988) developed a numerical model of tidal heights and cross section–averaged velocities for all of Puget Sound, tuning the bottom friction to reproduce observed M_2 heights and phases. Their prediction of velocity averaged across a section between TTP and Vashon Island, U_T, will be used to map the times of our observations onto a tidal time; U_T is a function of time only. To avoid tidal aliasing, we will only present microstructure section data taken within a two-hour window centered on the time that the ship crossed the TTP ridge.

Background conditions during the cruise come from surface meteorological and oceanographic parameters recorded aboard the *Thompson* at 5-s intervals. Hourly precipitation data from the Seattle-Tacoma International Airport, the closest source for such observations (6.3 km east of TTP, at 137-m elevation), were obtained from the National Climatic Data Center.

1) MICROSTRUCTURE MEASUREMENTS

During the nine sections across TTP, the turbulent and other properties of the flow were measured by repeat drops of the loosely tethered vertical profiler Chameleon (Moum et al. 1995) developed at Oregon State University. Because it can profile to the ocean floor, the measurements include the bottom boundary layer. The median spacing between Chameleon drops was 107 m, though the spacing varied between sections depending

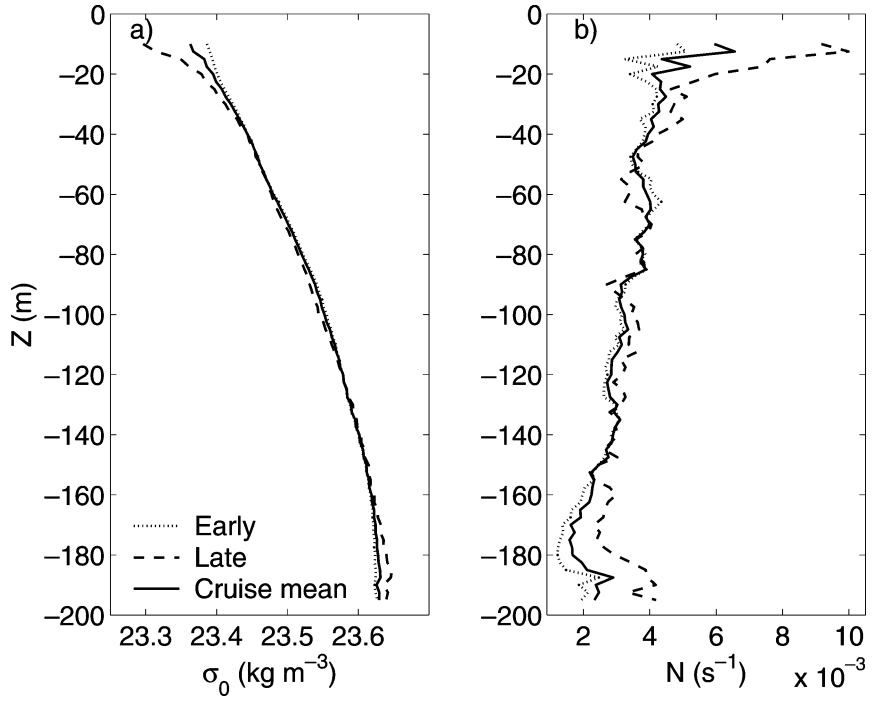

FIG. 4. (a) Profiles of potential density, σ_0, vs depth. Data taken in deep water north of TTP were averaged from early (late) in the cruise, before (after) storm onset; the overall mean that was used to initialize the numerical model is also shown. (b) Corresponding profiles of N.

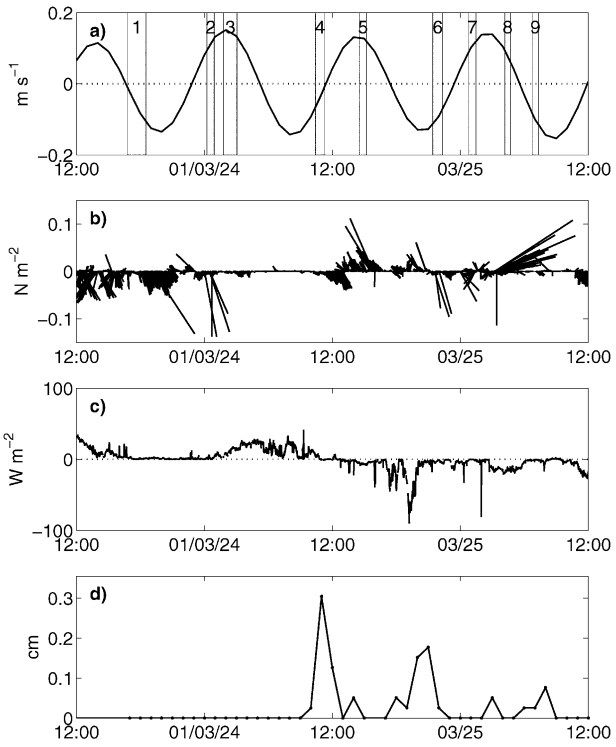

FIG. 5. Environmental conditions during the Chameleon surveys. (a) The predicted tidal currents, U_T, are plotted vs time [Pacific standard time (PST)] with the nine Chameleon sections labeled (gray bars). (b) A storm moved into the area around noon on 24 Mar and the wind stress vector is shown as a stick plot. (c) The sum of the shipboard sensible and latent heat fluxes, and (d) hourly precipitation.

on the ship speed and bottom depth. Near-surface observations are contaminated by the ship's wake, and so the first 10 m of data are discarded. The probe carries an array of instruments to measure temperature with a typical vertical resolution of 2 cm, and ~10 cm resolution for conductivity, from which salinity was calculated; these were later averaged to 1 m. Estimates of the turbulent dissipation rate ε were made at 1-m increments based on the velocity fluctuation measurements by airfoil shear probes (Osborn and Crawford 1980).

The Chameleon observations were used to estimate components of the drag at TTP. We can express the total boundary drag along a section as the sum of three terms: $D = D_{\mathrm{BBL}} + D^{\mathrm{int}}_{\mathrm{FORM}} + D^{\mathrm{surf}}_{\mathrm{FORM}}$, where D_{BBL} is the frictional drag from the bottom boundary layer in the direction of the section integrated over that section. The other two terms represent the form drag and are divided (based only on observational necessity) into internal form drag associated with pressure perturbations due to the deformation of isopycnals ($D^{\mathrm{int}}_{\mathrm{FORM}}$), and external form drag associated with pressure perturbations due to deformation of the surface height field ($D^{\mathrm{surf}}_{\mathrm{FORM}}$). The Chameleon data could only be used to estimate D_{BBL} and $D^{\mathrm{int}}_{\mathrm{FORM}}$. The along-section component of the form drag per unit width W of the bump is calculated as

$$\frac{D^{\mathrm{int}}_{\mathrm{FORM}} + D^{\mathrm{surf}}_{\mathrm{FORM}}}{W} = -\int_{X_1}^{X_2} p_B \frac{d\zeta}{dx'}\, dx', \qquad (2.1)$$

where the product of pressure at the ocean bottom, p_B, and the local, along-section topographic slope, $d\zeta/dx'$, is integrated along the track between the endpoints X_1 and X_2 (Fig. 3), which have the same bottom depth. The along-track coordinate is x' and is at an angle to the along-channel direction in the case of the Chameleon sections. Its origin is defined to be at the TTP crest. Drag is negative when it slows a flow of positive sign, here defined to be flooding/southward for along-channel flow. In order to calculate p^{int}_B (that portion of p_B associated with isopycnal displacement), we assume the flow is hydrostatic (perhaps questionable near the 1:5 slope), and integrate

$$p^{\mathrm{int}}_B = \int_{\zeta}^{z_0} g\rho\, dz, \qquad (2.2)$$

from the bottom to a specified near-surface position $z_0 = -10$ m. Then (2.2) is used in (2.1) to obtain $D^{\mathrm{int}}_{\mathrm{FORM}}$. The pressure per unit frontal area is calculated as $D^{\mathrm{int}}_{\mathrm{FORM}}/(WH_T)$ where H_T is the height of the obstacle (Fig. 3), which is about 100 m at the section's location. The barotropic form drag cannot be evaluated from the Chameleon dataset, though a calculation will be made from the results of the numerical simulation.

The frictional drag was estimated from the Chameleon ε measurements following Dewey and Crawford (1988). Within the log layer, skin friction is equal to the stress at any height within the layer

$$\tau_0 = \rho u_*^2, \qquad (2.3)$$

where u_* is the friction velocity. Within the layer, the balance between the rate of turbulent kinetic energy production by the mean shear $\partial U/\partial z$ and dissipation is written as

$$-\overline{u'w'}\frac{\partial U}{\partial z} = \varepsilon, \qquad (2.4)$$

where $-\overline{u'w'} \equiv u_*^2$ is the vertical Reynolds stress. If we substitute the ''law of the wall'' relation for the mean shear, $\partial U/\partial z = u_*/kz$, using the von Kármán constant $k \cong 0.4$, we obtain

$$u_* = (\varepsilon kz)^{1/3}. \qquad (2.5)$$

To make an estimate of skin friction from each Chameleon drop, we averaged the first two estimates of ε above the bed with the assumption that they were within the log layer. An along-track average was made between X_1 and X_2 to estimate the skin friction for each section. To obtain the skin friction per unit frontal area, the along-track average was multiplied by the distance between X_1 and X_2 then divided by H_T.

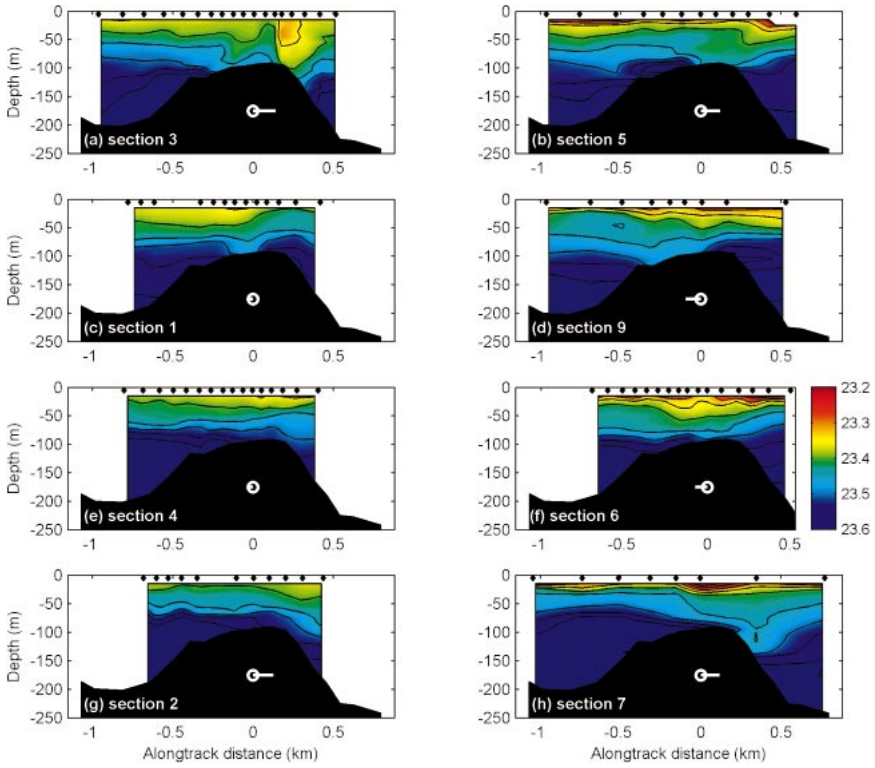

FIG. 6. Sections of observed potential density (color scale; contour interval is 0.05 kg m^{-3}) on eight Chameleon sections (Fig. 2). The perspective is from offshore looking toward the TTP ridge, which is centered at ~0 km in the along-track coordinate system. Drop locations are shown as black diamonds. Sections on the left (right) were taken before (after) an intrusion of low-density surface water. As one moves down the rows of panels, the sections progress through a tidal cycle beginning with max flood. The predicted tidal velocity, U_T, is shown in each panel as a white line emanating from a circle; its amplitude can be read from the horizontal axis in units of meters per second. A spectacular surface-intensified lee wave is apparent in (a).

A second motivation for making microstructure measurements is to estimate the turbulent buoyancy flux, which provides a measure of the enhanced diapycnal mixing due to the TTP ridge. The buoyancy flux is derived from the Chameleon observations following Osborn (1980). For a balance between turbulence production, dissipation and loss to buoyancy, he defined an upper bound on buoyancy flux, F_B, to be

$$F_B \leq \Gamma \varepsilon, \tag{2.6}$$

where the flux coefficient $\Gamma = 0.2$, based on laboratory results and observations. In accordance with many pre-

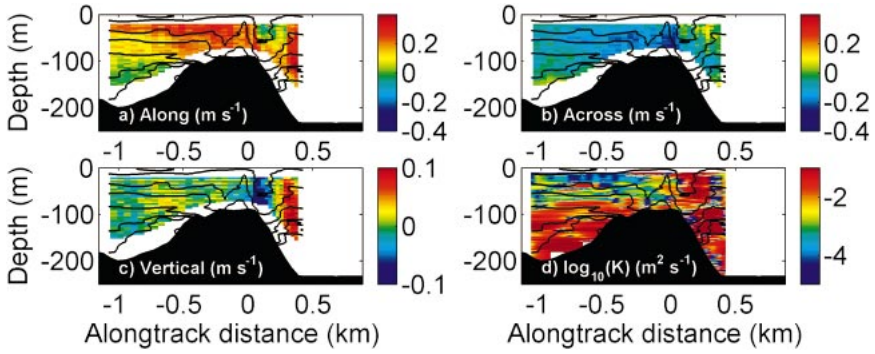

FIG. 7. For section 3 containing the lee wave, observed (a) along-channel, (b) across-channel, and (c) vertical velocity components are plotted. (d) The $\log_{10}$ of vertical eddy diffusivity κ. Potential density contours from Fig. 6 are overlain.

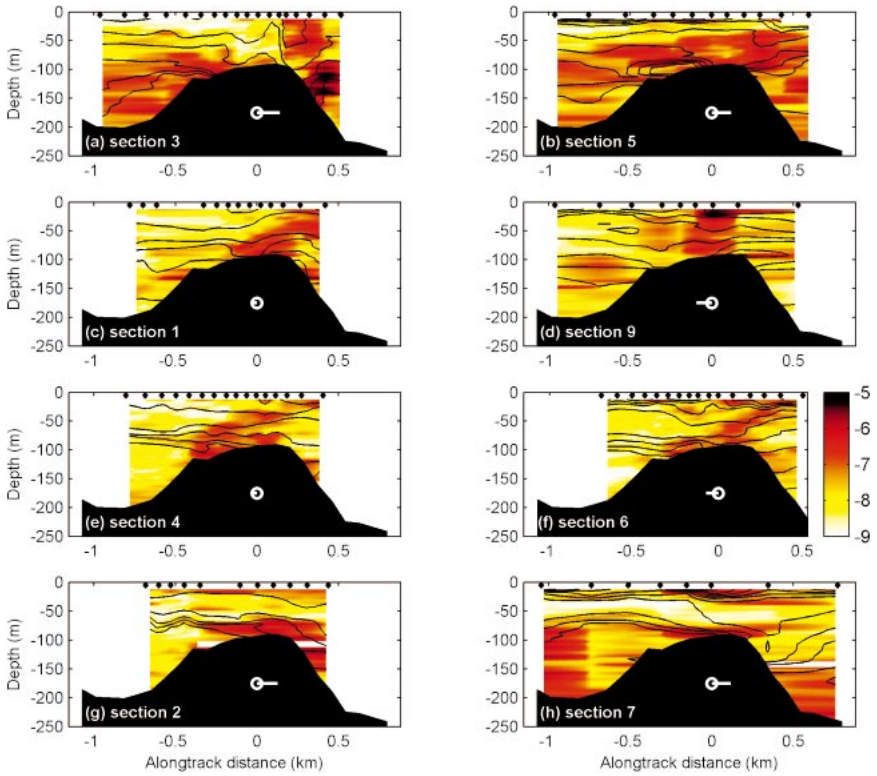

FIG. 8. Sections of the $\log_{10}$ of the observed turbulent buoyancy flux (color scale; W kg^{-1}) on the same Chameleon sections and along-track coordinate as in Fig. 6. Potential density contours from Fig. 6 are overlain. The strongest buoyancy flux is near the ridge, or in its lee, during max flood currents, especially in (a).

vious observational studies (e.g., Nash and Moum 2001), we approximate $F_B \sim 0.2\varepsilon$ but note that the actual value may be a function of the age of an overturn (Smyth et al. 2001) or the Richardson number (Peters and Bokhorst 2001). The buoyancy flux may also be written in terms of eddy diffusivity κ as

$$F_B = \kappa N^2,$$

where

$$N = \left(-\frac{g}{\rho_0} \frac{\partial \rho}{\partial z} \right)^{1/2}, \tag{2.7}$$

where g is gravity, ρ is density, and ρ_0 is a constant reference density.

2) CURRENT MEASUREMENTS

The *Thompson* carried an RDI 153-kHz narrowband acoustic Doppler current profiler (ADCP), which collected profiles of water velocity at 4-m vertical resolution. Velocity observations within 10 m of the surface were contaminated by the ship's motion, while near-bottom data within 15% of the total water depth were contaminated by sidelobe reflections; both were discarded. To reduce noise, velocity profiles were smoothed in time to ~2 min based on an analysis of the data's noise level.

To profile velocity at a fixed location throughout the cruise, a bottom-mounted RDI 300-kHz broadband ADCP was deployed near the tip of TTP at 43-m depth. Data were recorded at 60-s time resolution and in 2-m vertical bins. Near-surface data were discarded because of sidelobe reflections. A second moored ADCP was deployed farther offshore in 210 m of water by R. Dewey, University of Victoria. Locations for both are shown in Fig. 2b.

b. Model setup

To better understand the flow field at TTP, we performed a numerical simulation on the domain shown in Fig. 2b. As outlined below, the setup is somewhat idealized, and we seek qualitative rather than exact agreement with observed features. The model allows us to calculate the total frictional and form drag on TTP, whereas the microstructure observations only give these on a 2D section. Using the bathymetry of a 9 km by 8 km section of Main Basin that contains TTP, we interpolated the north and south edges of this section to artificially create a reentrant channel. This avoids the difficulties of open boundaries, and in fact we lack the

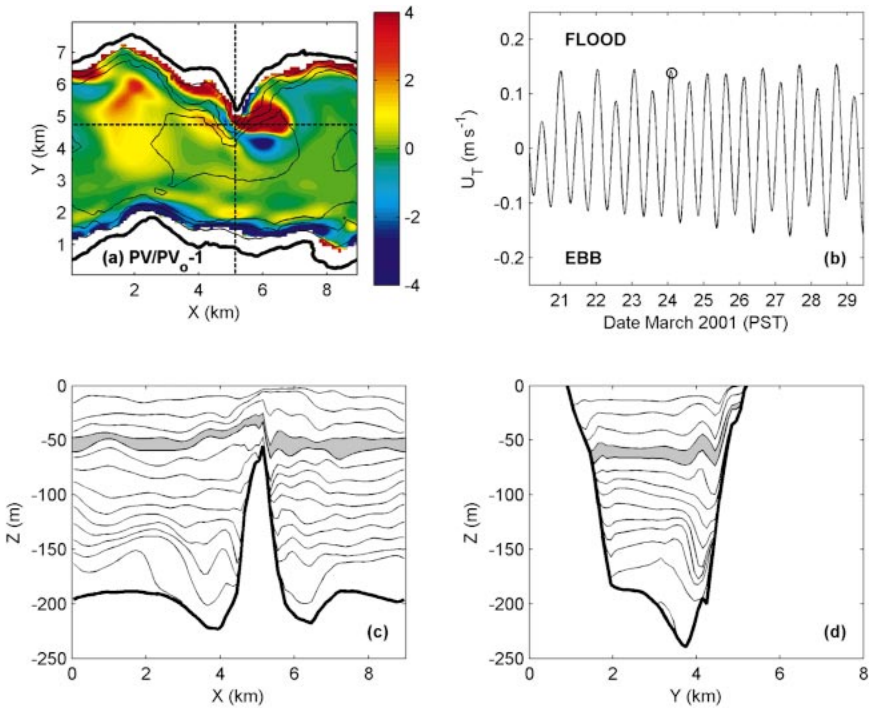

FIG. 9. Typical model output fields at a time close to max flood (flow to right). (a) The normalized potential vorticity of the fifth layer from the top. (b) The predicted tidal velocity for the entire run, with the time of (a) shown as a circle. The distortion of isopycnal layer interfaces is plotted for (c) along-channel and (d) across-channel sections, on the dashed lines in (a). The layer from (a) is shaded gray. A strong cyclonic or ''flood'' (red) eddy has just being released from TTP with an older ''ebb'' (blue) eddy offshore of it. The flood eddy is accompanied by large isopycnal displacements. The contour interval between density interfaces is not constant because all layers are initially 12 m thick, but the stratification is greater near the surface.

data to adequately specify properties at the boundaries. The use of a reentrant channel is reasonable for physical processes which are confined in space during the time period of interest; recently, periodic model boundary conditions were employed with good success by Oke et al. (2002) for coastal flow. Near TTP, the physical process of greatest importance is the tidal advection of eddies generated at the headland. Because the tidal excursion near TTP is ~3 km, eddies are not likely to be affected by the reentrant domain for at least a few tidal cycles. We use the hydrostatic Hallberg Isopycnic Model (HIM; Hallberg and Rhines 1996), with a Richardson number–dependent turbulence parameterization (Hallberg 2000). This gives the rate of turbulent entrainment through an interface as

$$w_e = \begin{cases} \Delta u \dfrac{0.1 - 0.1\mathrm{Ri}}{1 + 5\mathrm{Ri}} & \mathrm{Ri} < 1 \\ 0 & \mathrm{Ri} \geq 1, \end{cases} \tag{2.8}$$

where Δu is the velocity difference across layers, and Ri is the bulk Richardson number, defined as

$$\mathrm{Ri} = \frac{g'h}{\Delta u^2}. \tag{2.9}$$

The reduced gravity is $g' = g\Delta\rho/\rho_0$, where $\Delta\rho$ is the density step across an interface and h is the average thickness of adjacent layers. This class of parameterizations has been used by Price and Baringer (1994) to model overflow plume entrainment and is based on Turner (1986). It is designed for relatively high-energy flows, but we judge that the mixing levels at TTP are sufficiently high. In our model setup there was also a background diffusivity of 10^{-6} m^2 s^{-1}, but it had no dynamical importance. This model has proven to be useful for problems involving stratified flow over rough topography (MacCready and Pawlak 2001). The horizontal resolution is 100 m, and adequate vertical resolution was achieved by 20 isopycnal layers, each initially 12 m thick. The density step across layers varies with depth to match the average stratification over the period of Chameleon observations (Fig. 4a). Since this type of model does not inherently place high vertical resolution near boundaries, it does not in general resolve the details of the bottom boundary layer, unlike a model with a terrain-following coordinate system. Instead, the bottom stress is calculated using a quadratic drag law, with drag coefficient $C_D = 2.5 \times 10^{-3}$ based on the interpolated velocity averaged over the bottom 15 m. The bottom stress is then distributed in the water column

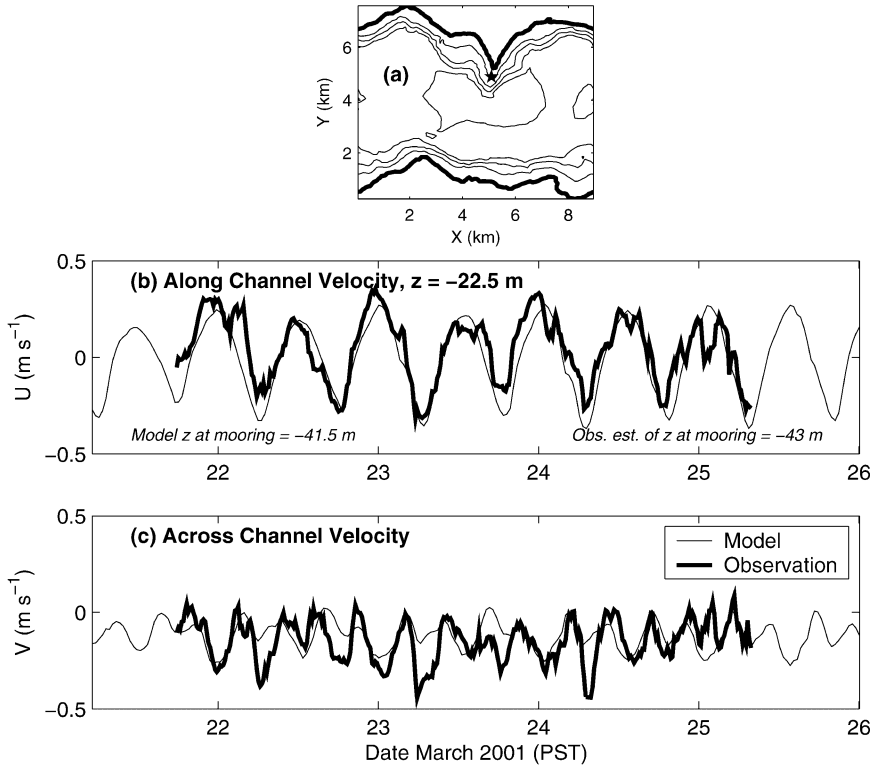

FIG. 10. Comparison of model and observed horizontal currents at middepth near the top of the ridge. (a) The mooring location and time series of (b) along-channel currents and (c) across-channel currents. There is strong amplification of the along-channel current by the ridge, and the flow has a component into the channel during both flood and ebb, indicative of horizontal flow separation.

by diapycnal fluxes, which are governed by the turbulence parameterization. This gives rise to boundary layers of realistic thickness where the vertical resolution is great enough, although here the boundary layers are not well resolved.

The sole dynamical forcing is a body force designed to reproduce the local along-channel tidal velocity, U_T, predicted by the Lavelle et al. (1988) model. The across-channel tidal velocity component, V_T, is 0 since there is no net across-channel transport. The body force was incorporated into the model as follows. First, we constructed an analytical version of U_T by fitting it with six tidal constituents (M_2, S_2, N_2, K_1, O_1, and P_1) for a 28-day time period around the cruise. The analytical form had less than 6% rms difference from the original signal. The along- and across-channel body force was then calculated from the equations

$$\frac{\partial U_T}{\partial t} - fV_T = \varphi^x \quad \text{and} \quad \frac{\partial V_T}{\partial t} + fU_T = \varphi^y. \quad (2.10)$$

A horizontal, time-dependent acceleration (φ^x, φ^y) is generated in the model by a fictitious body force, obtained as an integral of (2.10). This force is analogous to that due to a gradient of the surface height field, which is constant over the numerical domain, a reasonable approximation for this region of Main Basin. In the absence of irregular topography and friction, this form of forcing would exactly reproduce the desired along-channel velocity, U_T. With realistic bathymetry and boundary stress, there is net drag acting on (2.10), which would cause the resulting volume-average of U_T to have smaller amplitude than desired, and some phase lead. We proceed assuming that these are small, and rely on comparisons with current-meter observations to assess whether the forcing is reasonably correct. As in the observations, U_T will be used to map the model output onto a tidal time.

The model simulation was started from rest at a time when the predicted tidal velocity was 0, and was run for 216 lunar hours (a lunar hour is defined as 12.42/12 hours). The model was run for 83 lunar hours before the first Chameleon section, at which time the fields were reasonably spun up, while the stratification had not yet been mixed away.

3. Results

a. Observations

The surveys occurred during a time of spring tides with low diurnal inequality (Fig. 5a), based on the pre-

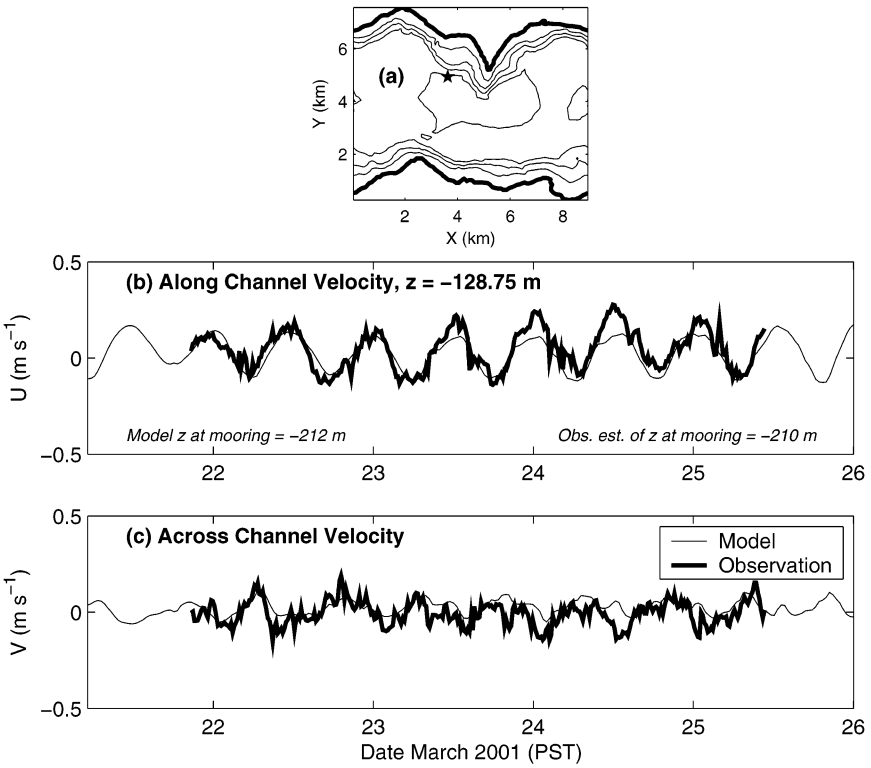

FIG. 11. Comparison of model and observed horizontal currents at middepth away from the ridge. (a) The mooring location; (b) along-channel currents and (c) across-channel currents vs time. After noon on 23 Mar the observed flow develops some flood dominance (positive *u*).

diction of Lavelle et al. (1988). Wind stress was generally southward in the first half of the cruise, turning northward and increasing around noon on 24 March (Fig. 5b) as a storm moved into the region. The wind reversal coincided with significant near-surface increase in stratification between the time of sections 4 and 5 due to both an increase in turbulent heat flux from the atmosphere into the surface layer (negative values in Fig. 5c) and to the addition of freshwater from precipitation (Fig. 5d). The effects on stratification are apparent in Fig. 4b, where average N in the upper 20 m approximately doubled after the storm.

CHAMELEON SECTIONS

Figure 6 shows the evolution of the density field along the Chameleon track (Fig. 2b), using an along-track coordinate which is 0 at the TTP ridge. Each row of Fig. 6 pairs sections taken during the same point in the tidal cycle, such as section 3 and section 5 from max flood; sections in the left column were recorded before the storm-related strengthening of near-surface stratification while sections on the right were taken afterward. Beginning with max flood, the tidal time increases down the rows.

Considering first the less-stratified case (left column), a sharp 50-m dip in the isopycnals occurs downstream (south) of the bump during maximum flood (Fig. 6a); dense fluid heaps up on its upstream side. During early ebb (Fig. 6c), the isopycnals relax to form a moderate depression over the bump. During late ebb, middepth isopycnals deepen downstream (north) of the bump (Fig. 6e). During early flood (Fig. 6g), a broad depression forms again on the downstream side of the bump. With the onset of greater surface stratification following the storm (right column), the density field alters. The most significant change is the lack of a sharply defined depression downstream of the bump during max flood (Fig. 6b). During late ebb (Fig. 6f), isopycnals dip across the bump as they did in the less-stratified case, but over a shorter distance. During early flood (Fig. 6h), the asymmetry of isopycnals across TTP is again apparent.

A dominant feature from the observations is the sharp isopycnal depression in section 3, taken during max flood in less-stratified conditions (Fig. 6a). The velocity fields from section 3 are displayed in Fig. 7. Significant along- and across-channel velocity shear is collocated with the isopycnal depression (Figs. 7a and 7b). Downward vertical velocity exceeds 6 cm s^{-1} in the dip, with similar upward magnitudes farther downstream (Fig. 7c). These flow features occur over a relatively short 100-m along-track distance and are interpreted to be associated with a standing lee wave combined with a

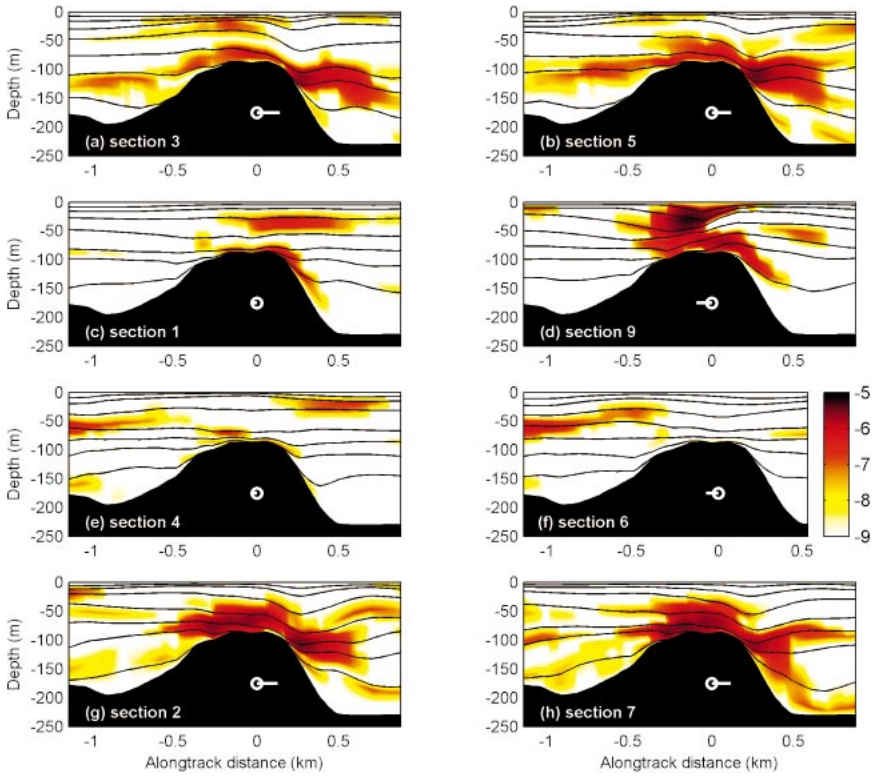

FIG. 12. Numerical model sections of the $\log_{10}$ of turbulent buoyancy flux (color scale; W kg^{-1}) on the same Chameleon sections as shown in Figs. 6 and 8. Potential density contours with the same contour interval as Figs. 6 and 8 are overlain. The model shows clearer intensification of the mixing near the ridge at times of maximum currents when compared with the observations. The background model buoyancy flux is much smaller.

headland eddy. Eddy diffusivity values [Eq. (2.7)] are exceptionally high in the isopycnal depression (Fig. 7d).

The less-stratified conditions in section 3 may be more favorable to flow ''over'' the bump and hence lee wave formation than those of section 5. Both are from maximum flood. The slope Froude number, $\mathrm{Fr}_{\mathrm{slope}}$, is defined in MacCready and Pawlak (2001) to be

$$\mathrm{Fr}_{\mathrm{slope}} = U_T[LN \sin(a)]^{-1}, \qquad (3.1)$$

where the along-channel topographic scale L of TTP is 500 m based on a Gaussian fit to the plan-view topography, and the angle, a, of the sloping sidewalls of TTP is $\sim 11°$. For $\mathrm{Fr}_{\mathrm{slope}} > 0.5$ (as might be found in weak stratification), MacCready and Pawlak (2001) showed that flow takes the shortest path over a sloping ridge while for $\mathrm{Fr}_{\mathrm{slope}} < 0.5$ (strong stratification), the flow is restricted to nearly horizontal motion and passes around the obstacle. This theory was developed for linear disturbances on an infinite, planar slope with constant N, whereas here the flow is clearly nonlinear, $\mathrm{Fr}_{\mathrm{slope}}$ varies with depth, and there is a free surface. Nonetheless, (3.1) may still serve as a guide if the flow is strongly in either the ''flow around'' or ''flow over'' regime. At 20 m beneath the sea surface, section-averaged values of $\mathrm{Fr}_{\mathrm{slope}}$ at TTP fall between 0.3 and 1 before the increase of near-surface stratification and 0–0.5 afterward, suggesting that the flow is near the transition between the different flow types and both headland eddies and a lee wave might form, as diagrammed in Fig. 1. Both would contribute to form drag.

The enhancement of mixing at TTP is seen in Fig. 8, which presents the buoyancy flux, F_B, inferred from the Chameleon dissipation measurements according to (2.6); F_B is patchy, but is strongest near the ridge. The greatest values occur in the lee wave in section 3 (Fig. 8a).

b. Model

Typical model flow fields are plotted in Fig. 9. It can be seen that TTP causes both a strong tidal headland eddy and significant deformation of isopycnals reminiscent of a lee wave. The normalized potential vorticity, q, in Fig. 9a is defined to be

$$q = \left[\frac{\left(\dfrac{\partial v}{\partial x} - \dfrac{\partial u}{\partial y} + f\right)h^{-1}}{f(h_{t=0})^{-1}}\right] - 1, \qquad (3.2)$$

where (u, v) are the horizontal components of velocity,

f is the Coriolis parameter, h is the layer depth, and t is time. The headland eddies survive long enough to interact with the opposite-signed eddy of the following tide and may form dipoles. The relative longevity of these eddies may be due to the depth of the water, which makes the effect of bottom friction small. The interaction of such eddies has been found by Pawlak and MacCready (2002) to be an effective way of driving mean flow either toward or away from a point.

c. Model–data comparison

In order to validate the model and to extend the observational results, model–data comparisons were performed. A measure of model accuracy is shown in Figs. 10 and 11, where measured and modeled horizontal currents from two bottom-mounted ADCPs are plotted. Since there is little vertical structure, an arbitrary middepth level was chosen for the comparison. At both locations, the basic tidal signal in the model is correct in magnitude and phase. However, over the deeper mooring the observed current is more flood-dominant than the model (Fig. 11b), especially after noon on 23 March. This may be due to one of the low-frequency modes observed by Bretschneider et al. (1985). Directly on the headland (Fig. 10), distortion of the currents by the topography is apparent. There is strong amplification of the along-channel current (Fig. 10b). During both ebb and flood the across-channel flow is negative (Fig. 10c), which is clear evidence of flow separation. This phenomenon is the physical cause of an M_4 peak in the power spectrum of the across-channel flow (not shown). The classic representation of the flow through tidal ellipse parameters has limited applicability here because the time trace of the current vector more closely resembles a ''V'' than an ellipse. A clear limitation of the model is that it often misses the peak of the across-channel flow during ebb currents. From the comparisons above, we judge that the model captures the gross features of the flow, but during ebb tide the modeled jet may not separate from the tip of TTP at the correct angle. This may be due to inaccuracy in the model bathymetry; even a minor misrepresentation of the tip of TTP could cause an offset in the separation point. In deeper water away from TTP (Fig. 11), there is again evidence of flood dominance later in the record which is not captured by the model. Otherwise we can conclude that the model, despite its idealized forcing and reentrant setup, does a reasonable job of simulating the tidal currents and their deformation by the topography.

For comparison to the Chameleon density and F_B, comparable sections from the numerical model are plotted in Fig. 12. Model fields are interpolated horizontally onto the mean Chameleon track, and are taken from the half-lunar hour closest to a given Chameleon section. As in the observations, isopycnals dip downstream of the ridge and F_B is enhanced near the crest and along the slopes, especially during flood. However, the model

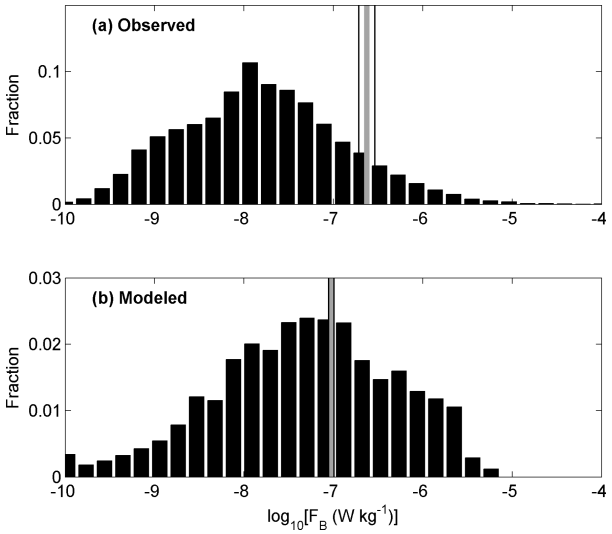

FIG. 13. (a) Histograms of the $\log_{10}$ of turbulent buoyancy flux inferred from the Chameleon observations and (b) from the numerical model. Means are shown as thick gray lines, with 95% bootstrap confidence intervals shown as thin black lines. The model histogram has a long, irregular tail of low values that fall off the left of (b) and account for 71% of the observations. The modeled fields were interpolated to 2-m vertical spacing, and values from layers thinner than this (typically isopycnal layers of essentially 0 thickness on the bottom) were excluded.

lacks the strong surface downwelling of Fig. 6a. As well, the model F_B tends to be more localized near the ridge, especially at maximum tidal currents. The model F_B drops off to lower values more rapidly than the Chameleon sections do, and the background model turbulence is less than observed.

Figure 13a shows a histogram of F_B from all the Chameleon sections, which has the nearly lognormal distribution expected for ε (e.g., Davis 1996) from which the estimate of F_B is derived [(2.6)]. The model mean F_B (0.93×10^{-7} W kg^{-1}; Fig. 13b) is only 39% of the observed (2.38×10^{-7} W kg^{-1}). This may be because the model resolution is too coarse to capture all the turbulence-generating scales, for example those of internal wave breaking, or the model turbulence closure may be at fault. Averaged onto potential density levels (Fig. 14), the model F_B compares well to observations over a broad middle density range but is too low in the lightest and heaviest density classes. The lack of near-surface mixing may be due to the absence of wind forcing in the model, while the lack of mixing in the deepest density classes remains unexplained. Over the model domain, 12% of the tidal energy lost to boundary processes goes into mixing, based on the time-integrated energy equation (not shown); however, the background stratification is not significantly altered over the simulation time period.

FORM DRAG AND FRICTIONAL DRAG

The model drag terms, integrated along the Chameleon section, are plotted against time in Fig. 15. On this

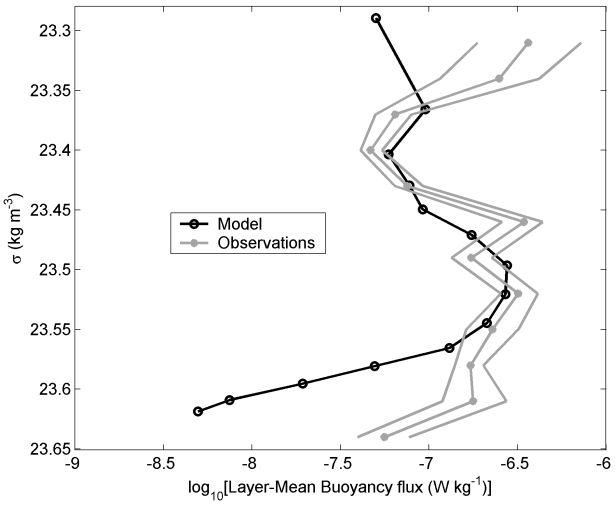

FIG. 14. Comparison of buoyancy fluxes interpolated onto potential density surfaces, for the Chameleon sections and the numerical model on the same sections. The 95% bootstrap confidence interval is shown for the Chameleon values. Density classes with very few observations (near the top and bottom) were excluded. There is good agreement in the middle density range, while in the light and heavy density classes the model underpredicts the buoyancy flux.

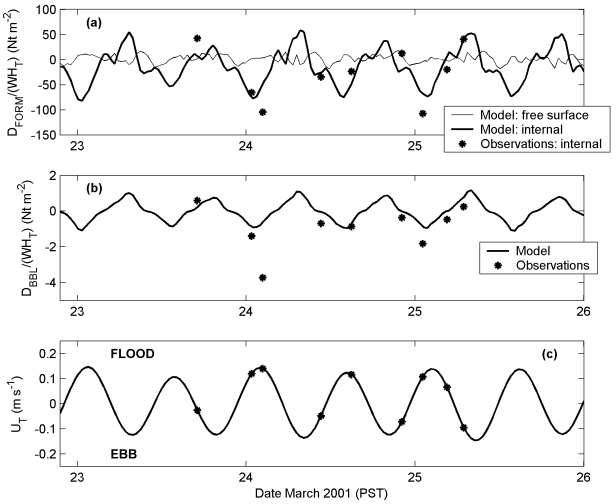

FIG. 15. (a) Form drag per unit frontal area, on the Chameleon section, comparing the model results (lines) with values from the nine Chameleon sections (asterisks). (b) The frictional drag per unit frontal area, and (c) the timing of the sections relative to U_T.

section $D^{\text{int}}_{\text{FORM}}$ dominates over $D^{\text{surf}}_{\text{FORM}}$ (Fig. 15a), and D_{BBL} is smaller than both by a factor of 10–50. The same integrated drag terms from the nine Chameleon sections are plotted as stars on Fig. 15. There is reasonable agreement between the model and observations, except that the model drag is low relative to the observations on approximately three occasions. One of these is section 3 (third star), when the model did not reproduce the large downwelling of light surface water in the lee of the ridge which would contribute to the form drag (Fig. 12a). The model also underpredicts the frictional drag for section 3, although there is no egregious mismatch in the velocity comparisons (Fig. 10) at that time. The results from Fig. 15 give reasonable confidence in the model form and frictional drag, so we turn next to the full volume-integrated drag budget, Fig. 16. Here the frictional drag is again negligible, having just 6% of the standard deviation of the form drag. The two form drag terms are now roughly equal in magnitude. We have found from numerical experiments (not shown) that the ratio $D^{\text{int}}_{\text{FORM}}/D^{\text{surf}}_{\text{FORM}}$ increases with distance from TTP. This is physically reasonable because the eddy (associated loosely with $D^{\text{surf}}_{\text{FORM}}$) is strongest in sections taken at the tip of TTP and in its lee. On the other hand, the baroclinic response is greater in deeper water.

In Fig. 16b we plot the volume-integrated rate of work performed by the sum of the model drag terms. Negative work results when the isopycnal tilt does not reverse when the tide turns; positive work is in the direction of the tide. As discussed previously, the flow at TTP leads the tide, as is typical at headlands. The work rate is calculated as $U_T \times D$ (MacCready et al. 2003), and we find that the time-averaged rate of conversion of barotropic tidal energy into waves, eddies, and eventually dissipation, is 0.72 MW.

4. Discussion

How can we tell if the time-averaged model work rate is reasonable? The only available comparison comes from the section-averaged tidal model of Lavelle et al. (1988). They used a linear drag on their section-averaged currents in order to match observed M_2 heights and phases throughout Puget Sound. The dynamics on a given cross section were governed by the equation

$$\frac{\partial U_T}{\partial t} = -g\frac{\partial \eta}{\partial x} - \frac{r}{\langle H \rangle}U_T, \tag{4.1}$$

where $\partial\eta/\partial x$ is the along-channel gradient of surface height, and $\langle H \rangle$ is the average depth on that section. They varied r as the tuning parameter, and in all the deep channels, including Main Basin where TTP is located, used $r = 2 \times 10^{-3}$ m s^{-1}. This is roughly equivalent to having a quadratic drag coefficient of 1–2 $\times$ 10^{-2}, or 4–8 times the values in regions without rough topography. We plot the work that would be done by this drag term in Fig. 16b. It is somewhat smaller in magnitude than our model results, does not have the phase lead relative to U_T, and does not change sign. Remarkably, however, its mean value, 0.86 MW, is quite close to the model mean.

One interpretation of the above result (admittedly generous to our model) is that our model and observations provide a physical explanation for the high friction Lavelle et al. (1988) found necessary to model the tides. The evidence strongly suggests that their estimated overall drag was essentially correct, but that the source of the drag was not friction. Rather, it was caused

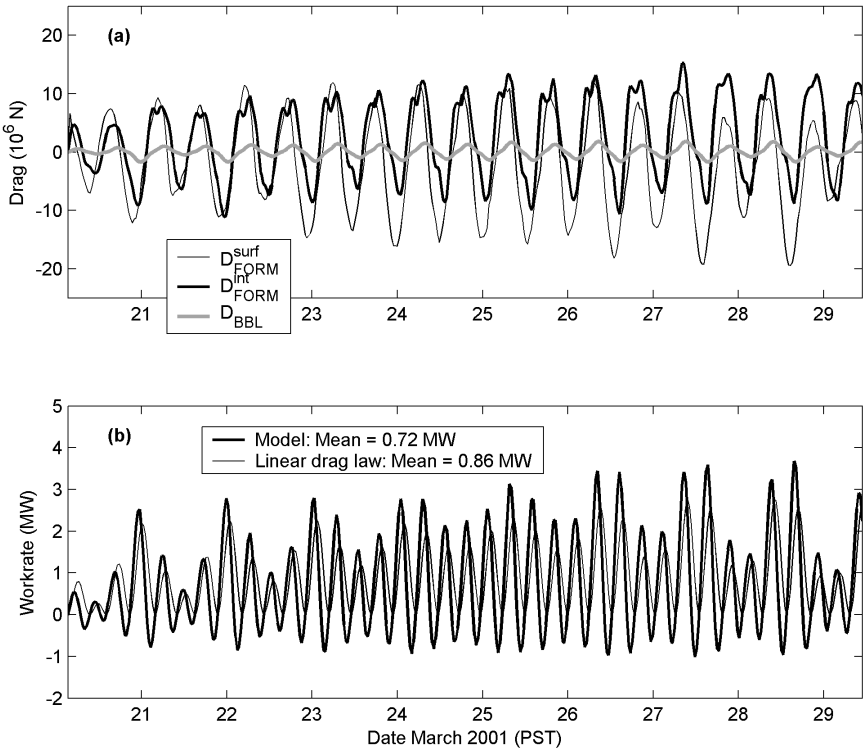

FIG. 16. (a) Volume-integrated drag terms vs time from the numerical model. The form drag terms are much larger than the frictional drag. (b) The rate of work performed by the sum of the model drag terms is compared with the work rate calculated from the linear tidal model of Lavelle et al. (1988).

predominantly by form drag on large features of rough topography such as TTP. It remains for future research to determine if these form drag results hold for other regions of Puget Sound, where topographic features like TTP are abundant and for rough coastal topography in general. Atmospheric models have recently begun to include parameterization of unresolved form drag due to orography (e.g., Lott and Miller 1997; Wood et al. 2001). The case study presented here suggests that similar attempts could improve oceanic models in regions of rough topography.

In the context of tidal dissipation throughout Puget Sound, TTP makes only a small contribution. Lavelle et al. (1988, their Fig. 35) find that 733 MW of tidal energy is dissipated on average in the sound. Of this, 513 and 78 MW are dissipated in Admiralty Inlet and Tacoma Narrows, respectively. These are two regions where tidal currents are greatly accelerated by narrowing and constriction of the channel, and have observed high dissipation rates (Seim et al. 1995; Seim and Gregg 1997). Within the section of Main Basin called East Passage, which contains TTP, Lavelle et al. (1988) estimate that only 5 MW of energy is lost from the barotropic tide, and as we showed above, they estimate that about 0.86 MW is lost in the 9-km segment of channel we have modeled. Thus the drag on TTP is not a dominant source of dissipation in Puget Sound as a whole, when compared with the huge losses at certain constrictions. However, within the large, slower-moving Main Basin, features such as TTP are likely to be important. Similar points are distributed every 5–10 km along the ~80 km length of Main Basin. Given that the tidal excursion is only a few kilometers there, such features could act as localized generators of turbulence and eddies, leading to more rapid dispersion of properties throughout the Basin.

The form drag mechanisms seen here have important implications for the mixing of tracers in coastal and near-boundary regions. Standard boundary layer drag enhances mixing only near the topography. This may be an inefficient generation mechanism for buoyancy flux, because stratification in the boundary layers is generally lower than in the interior. Form drag, on the other hand, tends to project its flow disturbances over the full depth of the water column, and over a volume similar to the product of the projected frontal area of the obstacle and the tidal excursion. Further, horizontal eddy structures shed by the obstacle (Fig. 9a) are an excellent means for constantly stirring fluid away from the mixing region which is replaced by new, unmixed fluid. Subsequent cruises followed the one presented here and made measurements to address the ''external'' component of form drag due to eddy formation at TTP (Pawlak et al. 2003). Analysis of these results will permit

the relative importance of eddies and waves in form drag generation at TTP to be evaluated.

5. Conclusions

We have presented observations of the density, turbulence, and currents at a headland in stratified tidal flow. At maximum flood, the flow structure resembles a lee wave, modified by the significant horizontal across-channel currents of a headland eddy. A numerical simulation was able to reproduce many aspects of the flow, although it only developed 39% of the average turbulent buoyancy flux inferred from observations. The two mechanisms for generating form drag, headland eddy formation and internal wave generation, appear to operate at TTP. The total drag of TTP on the tidal flow is due to the skin friction at the boundary, the ''internal form drag'' associated with the deformation of isopycnals and the ''external form drag'' due to the deformation of surface height. The internal form drag was calculated for nine sections across the ridge, and was found to be much greater than the skin friction. A volume-integrated drag budget from the model found that the skin friction was just 6% of the sum of the internal and external form drags, and thus form drag was the key process extracting energy from the barotropic tide. The fact that the form drag far exceeded simple boundary layer friction is consistent with previous tidal modeling in which a large linear drag was required to match observed tidal heights and phases.

Acknowledgments. We are indebted to the crew and captain of the R/V *Thomas G. Thompson* for their able work in a tight location. Ray Kreth, Mike Neeley-Brown, and Greig Thompson from OSU assisted with the field operations. Richard Dewey generously collected and processed data for one of the two moored ADCPs. Miles Logsdon and David Finlayson assembled the digital bathymetry of Puget Sound. Robert Hallberg (GFDL) provided almost daily assistance with the numerical modeling, along with David Darr (UW). We had many helpful conversations with Eric D'Asaro and Eric Kunze (UW), and Jonathan Nash (OSU). This work was supported by the ONR Scholar of Oceanography Award (PM and KE) and NSF Grants OCE-0099058 (PM and GP) and 9907854 (JM, JK, and AP).

REFERENCES

Baines, P. G., 1995: *Topographic Effects in Stratified Flows.* Cambridge University Press, 482 pp.

Barnes, C. A., and C. C. Ebbemeyer, 1978: Some aspects of Puget Sound's circulation and water properties. *Estuarine Transport Processes,* B. Kjerfve, Ed., University of South Carolina Press, 209–228.

Belcher, S. E., and J. C. R. Hunt, 1998: Turbulent flow over hills and waves. *Annu. Rev. Fluid Mech.,* **30,** 507–538.

Bretschneider, D. E., G. A. Cannon, J. R. Holbrook, and D. J. Pashinski, 1985: Variability of subtidal current structure in a fjord estuary: Puget Sound, Washington. *J. Geophys. Res.,* **90,** 11 949–11 958.

Davies, H. C., and P. D. Phillips, 1985: Mountain drag along the Gotthard section during ALPEX. *J. Atmos. Sci.,* **42,** 2093–2109.

Davis, R. E., 1996: Sampling turbulent dissipation. *J. Phys. Oceanogr.,* **26,** 341–358.

Dewey, R. K., and W. R. Crawford, 1988: Bottom stress estimates from vertical dissipation rate profiles on the continental shelf. *J. Phys. Oceanogr.,* **18,** 1167–1177.

Foreman, M. G. G., R. A. Walters, R. F. Henry, C. P. Keller, and A. G. Dolling, 1995: A tidal model for eastern Juan-de-Fuca Strait and the southern Strait of Georgia. *J. Geophys. Res.,* **100,** 721–740.

Garrett, C., P. MacCready, and P. B. Rhines, 1993: Boundary mixing and arrested Ekman layers: Rotating stratified flow near a sloping boundary. *Annu. Rev. Fluid Mech.,* **25,** 291–323.

Geyer, W. R., and R. Signell, 1990: Measurements of tidal flow around a headland with a shipboard acoustic Doppler current profiler. *J. Geophys. Res.,* **95,** 3189–3197.

Gill, A. E., 1982: *Atmosphere–Ocean Dynamics.* Academic Press, 662 pp.

Hafner, T. A., and R. B. Smith, 1985: Pressure drag on the European Alps in relation to synoptic events. *J. Atmos. Sci.,* **42,** 562–575.

Hallberg, R., 2000: Time integration of diapycnal diffusion and Richardson number–dependent mixing in isopycnal coordinate ocean models. *Mon. Wea. Rev.,* **128,** 1402–1419.

——, and P. B. Rhines, 1996: Buoyancy-driven circulation in an ocean basin with isopycnals intersecting the sloping boundary. *J. Phys. Oceanogr.,* **26,** 913–940.

Jayne, S. R., and L. C. St. Laurent, 2001: Parameterizing tidal dissipation over rough topography. *Geophys. Res. Lett.,* **28,** 811–814.

Klymak, J. M., and M. C. Gregg, 2001: Three-dimensional nature of a flow near a sill. *J. Geophys. Res.,* **106,** 22 295–22 311.

——, and ——, 2004: Tidally generated turbulence over the Knight Inlet Sill. *J. Phys. Oceanogr.,* **34,** 1135–1151.

Kundu, P. K., and I. M. Cohen, 2002: *Fluid Mechanics.* 2d ed. Academic Press, 730 pp.

Lavelle, J. W., H. O. Mofjeld, E. Lempriere-Doggett, G. A. Cannon, D. J. Pashinski, E. D. Cokelet, L. Lytle, and S. Gill, 1988: A multiply-connected channel model of tides and tidal currents in Puget Sound, Washington and a comparison with updated observations. NOAA Tech. Memo. ERL PMEL-84 (PB89-162515), 103 pp.

Ledwell, J. R., E. T. Montgomery, K. L. Polzin, L. C. St. Laurent, R. W. Schmitt, and J. M. Toole, 2000: Evidence of enhanced mixing over rough topography in the abyssal ocean. *Nature,* **403,** 179–182.

Lilly, D. K., 1978: A severe downslope windstorm and aircraft turbulence event induced by a mountain wave. *J. Atmos. Sci.,* **35,** 59–77.

Lott, F., and M. J. Miller, 1997: A new subgrid-scale orographic drag parameterization: Its formulation and testing. *Quart. J. Roy. Meteor. Soc.,* **123,** 101–127.

MacCready, P., and G. Pawlak, 2001: Stratified flow along a corrugated slope: Separation drag and wave drag. *J. Phys. Oceanogr.,* **31,** 2824–2839.

——, G. Pawlak, K. A. Edwards, and R. McCabe, 2003: Form drag on ocean flows. *Near Boundary Processes and their Parameterization: Proc. 'Aha Huliko'a Hawaiian Winter Workshop,* Honolulu, HI, University of Hawaii at Monoa, 119–130.

Moum, J. N., and J. D. Nash, 2000: Topographically induced drag and mixing at a small bank on the continental shelf. *J. Phys. Oceanogr.,* **30,** 2049–2054.

——, M. C. Gregg, R. C. Lien, and M. E. Carr, 1995: Comparison of turbulence kinetic energy dissipation rate estimates from two ocean microstructure profilers. *J. Atmos. Oceanic Technol.,* **12,** 346–366.

Nash, J. D., and J. N. Moum, 2001: Internal hydraulic flows on the continental shelf: High drag states over a small bank. *J. Geophys. Res.,* **106,** 4593–4611.

Oke, P. K., and Coauthors, 2002: A modeling study of the three-

dimensional continental shelf circulation off Oregon. Part I: Model-data comparisons. *J. Phys. Oceanogr.,* **32,** 1360–1382.

Osborn, T. R., 1980: Estimates of the local rate of vertical diffusion from dissipation measurements. *J. Phys. Oceanogr.,* **10,** 83–89.

——, and W. R. Crawford, 1980: An airfoil probe for measuring turbulent velocity fluctuations in water. *Air–Sea Interactions: Instruments and Methods,* F. Dobson et al., Eds., Plenum, 369–386.

Pawlak, G., and P. MacCready, 2002: Oscillatory flow across an irregular boundary. *J. Geophys. Res.,* **107**, 3036, doi:10.1029/2000JCO00596.

——, ——, K. A. Edwards, and R. McCabe, 2003: Observations on the evolution of tidal vorticity at a stratified deep water headland. *Geophys. Res. Lett.,* **30,** 2234, doi:10.1029/2003GL018092.

Peters, H., and R. Bokhorst, 2001: Microstructure observations of turbulent mixing in a partially mixed estuary. Part II: Salt flux and stress. *J. Phys. Oceanogr.,* **31,** 1105–1119.

Price, J. M., and M. O'Neil Baringer, 1994: Outflows and deep water production by marginal seas. *Progress in Oceanography,* Vol. 33, Pergamon, 161–200.

Schär, C., 2002: Mesoscale mountains and the larger-scale atmospheric dynamics: A review. *Meteorology at the Millennium,* R. Pearce, Ed., Academic Press, 29–42.

Seim, H. E., and M. C. Gregg, 1997: The importance of aspiration and channel curvature in producing strong vertical mixing over a sill. *J. Geophys. Res.,* **102,** 3451–3472.

——, ——, and R. T. Miyamoto, 1995: Acoustic backscatter from turbulent microstructure. *J. Atmos. Oceanic Technol.,* **12,** 367–380.

Signell, R. P., and W. R. Geyer, 1991: Transient eddy formation around headlands. *J. Geophys. Res.,* **96,** 2561–2575.

Smith, R. B., 1978: A measurement of mountain drag. *J. Atmos. Sci.,* **35,** 1644–1654.

Smyth, W. D., J. N. Moum, and D. R. Caldwell, 2001: The efficiency of mixing in turbulent patches: Inferences from direct simulations and microstructure observations. *J. Phys. Oceanogr.,* **31,** 1969–1992.

Thorpe, S. A., 1992: The generation of internal waves by flow over the rough topography of a continental slope. *Proc. Roy. Soc. London,* **439A,** 115–130.

Turner, J. S., 1986: Turbulent entrainment: The development of the entrainment assumption and its application to geophysical flows. *J. Fluid Mech.,* **173,** 431–471.

Wolanski, E., J. Imberger, and M. L. Heron, 1984: Island wakes in shallow coastal waters. *J. Geophys. Res.,* **89,** 10 553–10 569.

Wood, N., A. R. Brown, and F. E. Hewer, 2001: Parameterizing the effects of orography on the boundary layer: An alternative to effective roughness lengths. *Quart. J. Roy. Meteor. Soc.,* **127,** 759–777.